ISSN 1063-7788, Physics of Atomic Nuclei, 2023, Vol. 86, No. 6, pp. 1165–1172. © Pleiades Publishing, Ltd., 2023.
Russian Text © The Author(s), 2023, published in Yadernaya Fizika, 2023, Vol. 86, No. 6, pp. 672–680.

ELEMENTARY PARTICLES AND FIELDS
Experiment

Measuring the Neutron Timelike Electromagnetic Form Factor with the SND Detector

M. N. Achasov[1),2)], A. Yu. Barnyakov[1),2)], E. V. Bedarev[1),2)], K. I. Beloborodov[1),2)], A. V. Berdyugin[1),2)], D. E. Berkaev[1)], A. G. Bogdanchikov[1)], A. A. Botov[1)], T. V. Dimova[1),2)], V. P. Druzhinin[1),2)], V. N. Zhabin[1),2)], Yu. M. Zharinov[1)], L. V. Kardapoltsev[1),2)], A. S. Kasaev[1)], D. P. Kovrizhin[1)], I. A. Koop[1),2)], A. A. Korol[1),2)], A. S. Kupich[1),2)], A. P. Kryukov[1)], A. P. Lysenko[1)], N. A. Melnikova[1),2)], N. Yu. Muchnoi[1),2)], A. E. Obrazovsky[1)], E. V. Pakhtusova[1)], K. V. Pugachev[1),2)], S. A. Rastigeev[1)], Yu. A. Rogovsky[1),2)], S. I. Serednyakov[1),2)*], Z. K. Silagadze[1),2)], I. K. Surin[1)], Yu. V. Usov[1)], A. G. Kharlamov[1),2)], Yu. M. Shatunov[1)], and D. A. Shtol[1)]

Received June 29, 2023; revised June 29, 2023; accepted June 29, 2023

Abstract—Results are presented from measuring the $e^+e^- \to n\bar{n}$ cross section and effective neutron timelike form factor. Data are collected in 2020–2021 at the VEPP-2000 e^+e^- collider in the 1891 to 2007 MeV center-of-mass range of energies. The general purpose nonmagnetic SND detector is used to detect neutron–antineutron events. The time-of-flight approach is used to select $n\bar{n}$ events. The measured cross section is 0.4–0.6 nbn. The neutron form factor in the investigated range of energies varies from 0.3 to 0.2.

DOI: 10.1134/S1063778823060054

1. INTRODUCTION

The internal structure of nucleons is described by electromagnetic form factors. In the timelike region, they are measured according to the process of e^+e^- annihilation to nucleon–antinucleon pairs. The $e^+e^- \to n\bar{n}$ cross section depends on two form factors, electric G_E and magnetic G_M:

$$\frac{d\sigma}{d\Omega} = \frac{\alpha^2\beta}{4s}\left[|G_M(s)|^2\left(1+\cos^2\theta\right) + \frac{1}{\gamma^2}|G_E(s)|^2\sin^2\theta\right], \quad (1)$$

where α is the fine-structure constant; $s = E^2$ and $E = 2E_b$, where E_b is the beam energy and E is the center-of-mass (c.m.) energy; $\beta = \sqrt{1-4m_n^2/s}$; $\gamma = E_b/m_n$; m_n is the neutron mass; and θ is the polar angle of antineutron production. The total cross section has the form

$$\sigma(s) = \frac{4\pi\alpha^2\beta}{3s}\left(1+\frac{1}{2\gamma^2}\right)|F(s)|^2, \quad (2)$$

where we introduce an effective form factor $F(s)$:

$$|F(s)|^2 = \frac{2\gamma^2|G_M(s)|^2 + |G_E(s)|^2}{2\gamma^2+1}. \quad (3)$$

Ratio $|G_E/G_M|$ can be obtained by analyzing measured distribution cosθ in Eq. (1). At the threshold, $|G_E| = |G_M|$.

The latest results on the neutron form factor near the threshold were obtained in experiments 0n the VEPP-2000 e^+e^- collider with the SND detector [1]. The same work provided a list of earlier measurements. New data on energies above 2 GeV were obtained in [2] by the BESIII detector. In this work, we present recent SND results on the $e^+e^- \to n\bar{n}$ cross section and neutron timelike form factor with four times more integrated luminosity than the measurements in [1].

2. COLLIDER, DETECTOR, EXPERIMENT

The VEPP-2000 is a e^+e^- collider [3] operating in the range of energies from hadron threshold $E =$ 280 MeV to 2 GeV. The collider's luminosity above the nucleon threshold at 1.87 GeV is on the order of 5×10^{31} cm^{-2} s^{-1}. There are two collider detectors on the VEPP-2000: the SND and the CMD-3.

[1)]Budker Institute of Nuclear Physics, Siberian Branch, Russian Academy of Sciences, Novosibirsk, 630090 Russia.
[2)]Novosibirsk State University, Novosibirsk, 630090 Russia.
[*]E-mail: S.I.Serednyakov@inp.nsk.su

The SND (Spherical Neutral Detector) [4] is a non-magnetic detector consisting of a tracking system, a spherical NaI(Tl) electromagnetic calorimeter (EMC) and a muon detector (Fig. 1). The EMC is the main part of the SND used in $n\bar{n}$ analysis. The EMC is 34.7 cm thick (13.4 radiation lengths). The length of antineutron annihilation in NaI(Tl) varies with energies of several cm close to the $n\bar{n}$ threshold to $\sim$15 cm at the maximum available energy [5], so nearly all of the produced antineutrons are absorbed in the detector.

The EMC is used to measure the time of event arrival. A system of ash ADC modules [6] that measure the signal waveform has been installed on each of the 1640 EMC counters since 2019. The times and amplitudes of the signals in the counters are calculated when fitting the ash ADC output waveform. The time of an event is calculated as the energy weighted average time. The time resolution obtained with $e^+e^- \to \gamma\gamma$ events is around 0.8 ns.

This work presents an analysis of data with an integrated luminosity of 80 pb^{-1}, collected at eight energy points in the 1.891–2.007 GeV range of energies.

3. SELECTING $n\bar{n}$ EVENTS

The antineutron from an $n\bar{n}$ pair usually annihilates, producing pions, nucleons, photons, and other particles that deposit up to 2 GeV in the EMC. The neutron from an $n\bar{n}$ pair releases a small signal in the EMC that is barely visible against the background of the strong $n\bar{n}$ annihilation signal, so it is ignored. $n\bar{n}$events are reconsructed as multiphoton events.

The main features of $n\bar{n}$ events are the absence of charged tracks and photons from the region of collision and a strong imbalance in event momentum. To create the conditions for $n\bar{n}$ selection, we consider the sources of the background. These include the cosmic background, the background from processes of e^+e^- annihilation, and the background from the electron and positron beams in the collider.

Based on these features of the process $e^+e^- \to n\bar{n}$, conditions for selection are divided into three groups.

The first group contains conditions that suppress the background from events of e^+e^- annihilation. These include the condition of no charged tracks in an event, the limit on the total event momentum ($p/2E_b > 0.4$), and a limit on the transverse shower profile in the EMC [7] that must be wider than the one from the photons in the region of collision.

In the second group, the conditions of selection must suppress the cosmic background. These include the muon system veto, special conditions for analyzing the shape of energy deposition in the EMC, and removing cosmic events that pass through the muon veto [1]. These are basically cosmic showers in the EMC.

The third group of selection conditions contains a resriction on the total energy deposited in the EMC, $E_{\rm dep} > E_b$. This restriction almost completely suppresses the beam background, although the efficiency of detection is also reduced by around 20%.

The above selection conditions are similar to those described in [1]. The only difference is that there is no limit on the energy in the third layer of the EMC. This improves the efficiency of detection slightly, but it also increases the cosmic background. After imposing the described selection conditions, there are around 400 events/pb left for further analysis.

4. OBTAINING THE NUMBER OF $n\bar{n}$ EVENTS

The time spectra for selected data events are shown in Fig. 2. Zero time corresponds to events at the moment of beam collision. Three main components can be distinguished in the time spectrum shown in the figure: the beam background at $t = 0$; the cosmic background, uniform over time; and a delayed signal from $n\bar{n}$ events that is wide in time. The measured time spectra are fitted respectively according to the sum of these three components in the form

$$F(t) = N_{n\bar{n}} H_{n\bar{n}}(t) + N_{\rm csm} H_{\rm csm}(t) + N_{\rm bkg} H_{\rm bkg}(t), \quad (4)$$

where $H_{n\bar{n}}$, $H_{\rm csm}$ and $H_{\rm bkg}$ are the normalized histograms describing the time spectra for the $n\bar{n}$ signal, cosmic, and beam + physical backgrounds, respectively. $N_{n\bar{n}}$, $N_{\rm csm}$, and $N_{\rm bkg}$ are the corresponding event numbers obtained from the fit. The shape of beam + physical background time spectrum $H_{\rm bkg}$ is measured at energies below the $n\bar{n}$ threshold. Cosmic time spectrum $H_{\rm csm}$ is measured with the lower EMC threshold 0.9 E_b in coincidence with the muon system's signal.

A comparison of the time spectra in the data and MC gives a wider time distribution of the data for both $e^+e^- \to \gamma\gamma$ and $e^+e^- \to n\bar{n}$ events. For $e^+e^- \to \gamma\gamma$ events, this is due to the finite time resolution of our timing system [6], which is not adequately modeled. We therefore convolve the MC time spectrum using a Gaussian with $\sigma_{\gamma\gamma} = 0.8$ ns. Convolution for $e^+e^- \to n\bar{n}$ events is done with $\sigma_{nn} = 1.5$–2 ns, depending on the energy.

In addition to the above, we correct the MC $n\bar{n}$ time spectrum, since the shape of MC time spectrum $H_{n\bar{n}}$ does not describe data well. This discrepancy

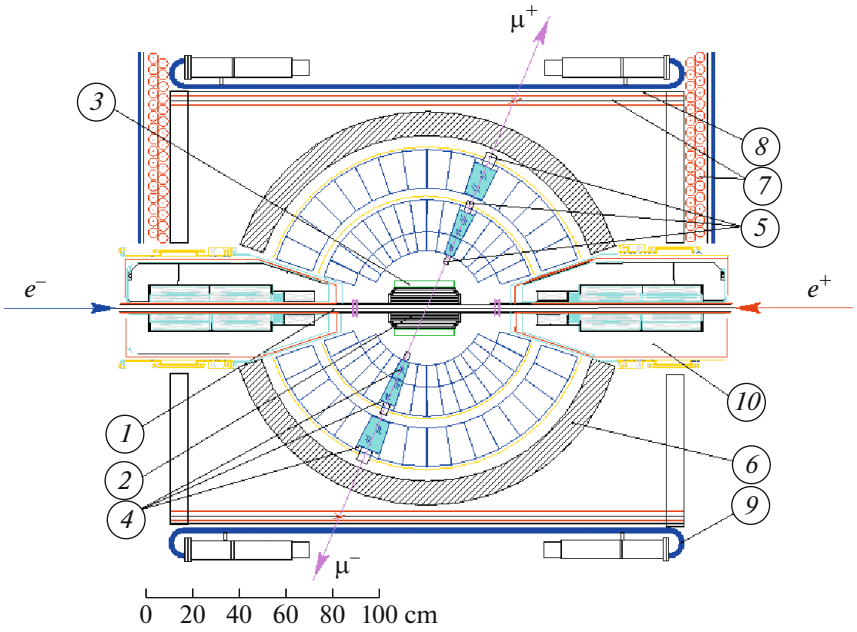

Fig. 1. SND detector, section along the beams: (*1*) beam pipe; (*2*) tracking system; (*3*) aerogel Cherenkov counters; (*4*) NaI (Tl) crystals; (*5*) vacuum phototriodes; (*6*) iron absorber; (*7*) proportional tubes; (*8*) iron absorber; (*9*) scintillation counters; (*10*) VEPP-2000 focusing solenoids.

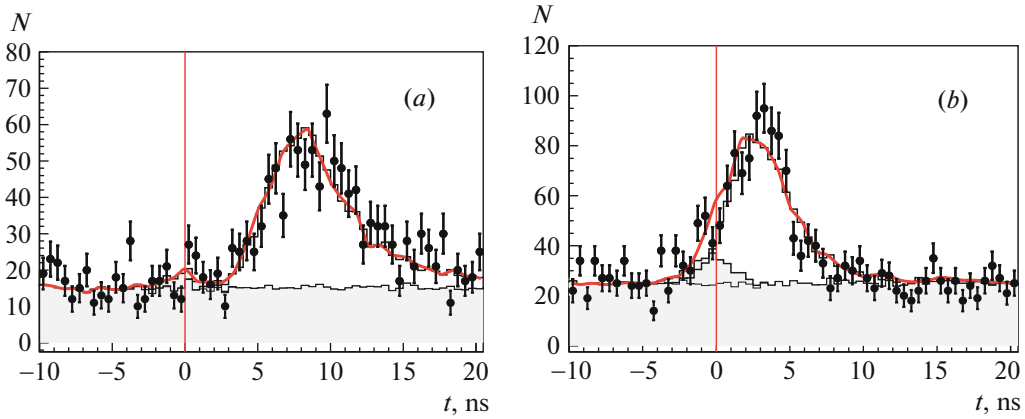

Fig. 2. Time distribution of selected data events (points with error bars) at $E_b = 945$ MeV (a) and at $E_b = 980$ MeV (b). Position $t = 0$ corresponds to the moment of beam collision. The wide peak to the right is the contribution from $n\bar{n}$ events. The shaded histogram shows the cosmic background (uniform over time) and beam background (peak at $t = 0$). The solid line is the result from fitting.

is explained by the incorrect relationship between the processes of antineutron annihilation and scattering in the MC, and by the incorrect description of annihilation products. To modify the MC time spectrum, separate MC time spectra are plotted for the first $\bar{n}$ interaction of annihilation and scattering. Annihilation yields time spectrum ($H^{an}_{n\bar{n}}$) close to exponential, while scattering has delayed and wider time spectrum ($H^{sc}_{n\bar{n}}$) with a non-exponential shape. The share of annihilation events in the MC was 33%. When fitting, the MC time spectrum was considered a linear sum of the two spectra described above: $H_{n\bar{n}} = \alpha H^{an}_{n\bar{n}} + (1-\alpha)H^{sc}_{n\bar{n}}$. Value α (the share of annihilation events) was the fit parameter. This turned out to be greater than in the MC: $\simeq$60%, and the degree of scattering fell to $\simeq$40%. The modified MC time spectrum describes the data well, as can be seen in Fig. 2.

Visible cross section σ_{dg} of the beam + physical background, obtained during fitting, is about 7 pb and does not depend appreciably on the beam's energy. The main contribution to σ_{dg} comes from processes with neutral kaons in the final state: $e^+e^- \to$

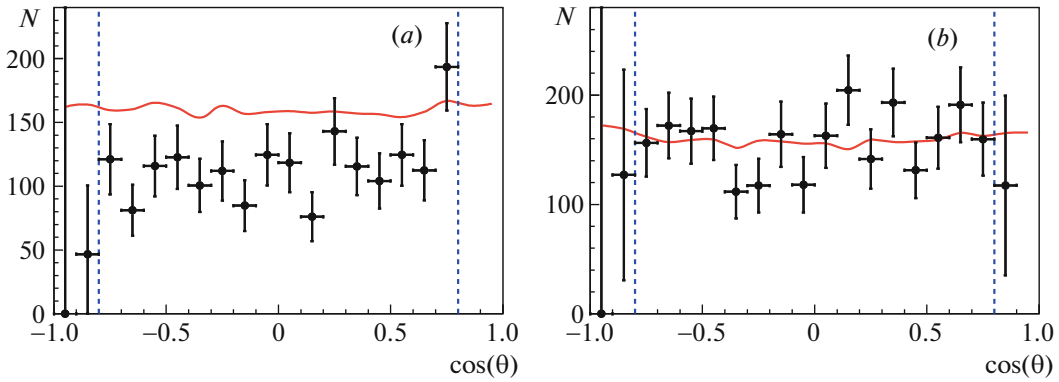

Fig. 3. Antineutron $\cos\theta_a$ distribution for data (points with error bars) and MC (horizontal line) at $E_b = 970$ MeV (a) and $E_b = 1000$ MeV (b). Dotted vertical lines correspond to the polar angle cutoff.

$K_SK_L\pi^0$, $K_SK_L\eta$ and others that are similar. The measured rate of the residual cosmic background has intensity ∼0.01 Hz, which corresponds to the suppression of the number of cosmic events passing through the hardware selection in the detector electronics by approximately 2×10^4 times.

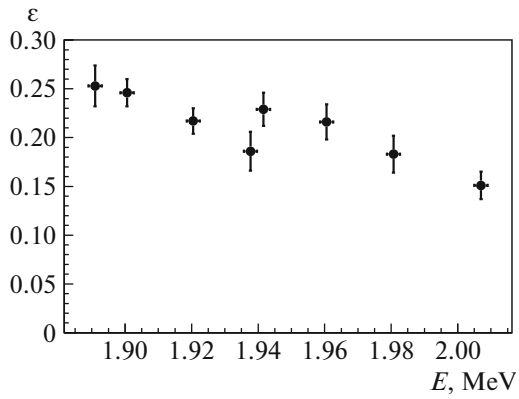

Fig. 4. Corrected efficiency of detection versus energy.

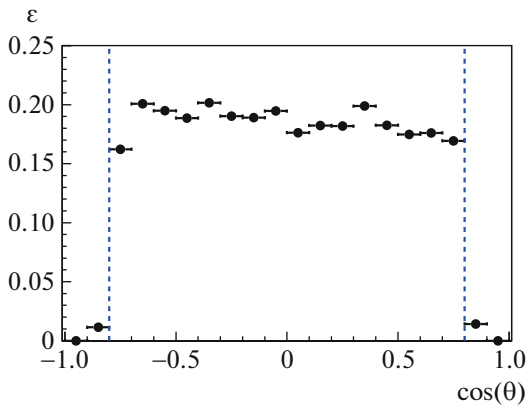

Fig. 5. MC efficiency of detection as a function of antineutron $\cos\theta$ at $E_b = 960$ MeV. Dotted vertical lines correspond to the polar angle cutoff.

Numbers of observed $n\bar{n}$ events are listed in Table 1. The total number is close to 6000. Table 1 shows only statistical errors of fitting. Sources of systemic error in the number of $n\bar{n}$ events include uncertainties in the magnitide and shape of the time spectrum of the beam and cosmic backgrounds. The error introduced by these sources is fifteen events at $E_b = 1000$ MeV and less than eight events at lower energies. These values are much lower than statistical errors in Table 1 and are ignored below.

5. ANGULAR DISTRIBUTION OF ANTINEUTRONS

Angle θ_n of antineutron production is determined by the direction of event momentum with an accuracy of around 5 degrees. The distribution over $\cos\theta_n$ for data and MC events is shown in Fig. 3. MC modeling was done using Eq. (1) under the assumption $G_E = G_M$ The efficiency of detection in selection interval $36° < \theta_n < 144°$ is 80%. We can see from Fig. 3 that the data and MC distributions agree with each other, confirming the MC angular model. It is also worth noting that earlier measurements of value $|G_E/G_M|$ [1] do not contradict hypothesis $G_E = G_M$ either.

6. EFFICIENCY OF DETECTION

Efficiency of detection ε versus energy under accepted selection conditions (Section 3) is shown in Fig. 4. In calculating ε, we used the MC model of process $e^+e^- \to n\bar{n}$ with the GEANT4 toolkit [8], version 10.5. The model also included beam energy spread ∼1 MeV and the emission of photons by the initial electrons and positrons. The model also considered non-operating detector channels and overlapping of the beam background and recorded events. Special superpositioning events were recorded and subsequently superimposed on MC events during the experiment using a pulse generator synchronized

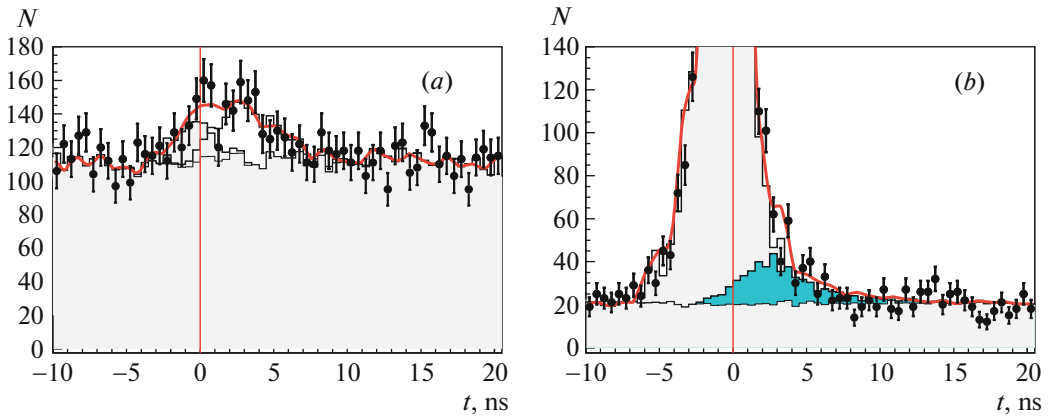

Fig. 6. Event time spectra with inverted selection conditions. (a) inverted 2-nd group cut at $E_b = 970$ MeV; (b) inverted 3-d group cut with $0.7E_b < E_{\rm cal} < E_b$ at $E_b = 960$ MeV. The lightly shaded histogram shows the background distribution. The darkly shaded histogram in the right plot is the $n\bar{n}$ contribution.

Table 1. Beam energy (E_b); integrated luminosity (L); number of selected $n\bar{n}$ events ($N_{n\bar{n}}$); factor allowing for radiative corrections and energy spread ($1+\delta$); corrected efficiency of detection (ε); measured $e^+e^- \to n\bar{n}$ cross section σ, and neutron effective form factor (F_n); quoted errors for N σ are statistical and systemic; the systemic uncertainty is quoted for the efficiency of detection; the combined statistical and systemic uncertainty are listed for F_n

	E_b, MeV	L, pb^{-1}	$N_{n\bar{n}}$	$1+\delta$	ε	σ, nbn	F_n
1	945.5	8.54	676 ± 37	0.746	0.253 ± 0.021	$0.420 \pm 0.023 \pm 0.036$	0.322 ± 0.016
2	950.3	8.86	834 ± 37	0.787	0.246 ± 0.015	$0.485 \pm 0.022 \pm 0.031$	0.301 ± 0.012
3	960.3	8.33	767 ± 35	0.840	0.217 ± 0.013	$0.506 \pm 0.023 \pm 0.032$	0.266 ± 0.010
4	970.8	8.07	718 ± 34	0.870	0.229 ± 0.017	$0.447 \pm 0.021 \pm 0.034$	0.230 ± 0.011
5	968.8	5.51	524 ± 34	0.870	0.186 ± 0.020	$0.589 \pm 0.039 \pm 0.065$	0.267 ± 0.017
6	980.3	7.70	654 ± 37	0.900	0.216 ± 0.018	$0.436 \pm 0.025 \pm 0.038$	0.216 ± 0.011
7	990.4	8.77	624 ± 38	0.920	0.183 ± 0.019	$0.422 \pm 0.026 \pm 0.045$	0.204 ± 0.013
8	1003.5	20.06	1075 ± 50	0.947	0.151 ± 0.014	$0.374 \pm 0.018 \pm 0.035$	0.186 ± 0.010

with the moment of beam collision. Efficiency of detection ε in Fig. 4 is corrected for the difference between the data and the MC. This correction is discussed below. Numerical values of efficiency are given in Table 1. The drop in ε along with energy can be explained by the energy dependence of the selection parameters, and by an increase in energy beyond the calorimeter. Figure 5 shows the efficiency of angular detection at beam energy $E_b = 960$ MeV.

Our measurement of the efficiency of detection is on the order of 20%. It is important to determine how correctly the proportion of events outside the selection condition was modeled. Corrections were calculated for the three groups of selection conditions described in Section 3. We inverted the selection conditions for each group and then calculated corresponding corrections δ for the efficiency of detection in each of eight energy points:

$$\delta = \frac{n_0}{n_0 + n_1} \frac{m_0 + m_1}{m_0}, \qquad (5)$$

where n_0 (n_1) is the number of $n\bar{n}$ events determined with standard (inverted) selections. These numbers were calculated while fitting the time spectra with Eq. (4), as was described in Section 4. Values m_0 and m_1 refer respectively to the numbers of MC modeling events. Examples of time spectra obtained with inverted selections are shown in Fig. 6.

The first group of selection conditions includes the requirement of no charged tracks in an event. When studying inverse selections, we assume there are central charged tracks with $D_{xy} > 0.5$ cm, where D_{xy} is the distance between the track and the axis of the beam. A possible background from related process $e^+e^- \to p\bar{p}$ should be noted here. Protons

Table 2. Beam energy (E_b); correction to efficiency of detection δ_1 from SND internal system; correction δ_2 from the SND external system; correction δ_3 from the EMC thresholds; correction δ_E from the lost EMC energy. Correction δ_t is the total correction

	E_b, MeV	δ_1	δ_2	δ_3	δ_E	δ_t
1	945.5	0.991 ± 0.022	1.292 ± 0.092	0.971 ± 0.038	1.005 ± 0.005	1.249 ± 0.102
2	950.3	0.977 ± 0.018	1.214 ± 0.062	0.985 ± 0.030	1.009 ± 0.009	1.179 ± 0.072
3	960.3	9.966 ± 0.019	1.077 ± 0.050	0.992 ± 0.028	1.012 ± 0.012	1.044 ± 0.062
4	970.8	0.949 ± 0.021	1.198 ± 0.061	0.980 ± 0.050	1.018 ± 0.018	1.134 ± 0.084
5	968.8	0.958 ± 0.027	1.031 ± 0.080	0.896 ± 0.044	1.018 ± 0.018	0.901 ± 0.097
6	980.3	0.997 ± 0.031	1.102 ± 0.073	0.986 ± 0.043	1.021 ± 0.021	1.106 ± 0.093
7	990.4	0.925 ± 0.033	1.131 ± 0.080	0.889 ± 0.041	1.024 ± 0.024	0.952 ± 0.099
8	1003.5	0.915 ± 0.024	1.065 ± 0.056	0.796 ± 0.028	1.028 ± 0.028	0.797 ± 0.073

and antiproptons in energy region $E_b > 960$ MeV yield central collinear tracks and are rejected by the requirement $D_{xy} > 0.5$ cm, along with events from other processes of e^+e^- annihilation with charged tracks. At $E_b < 960$ MeV, however, the protons and antiproptons are slow and stop at the collider's vacuum pipe. The antiproton annihilates with the production of charged tracks, which can have $D_{xy} > 0.5$ cm. But here too, background $e^+e^- \to p\bar{p}$ is suppressed by fitting the time spectrum, since the delay in annihilation is no more than 1 ns. Inverted selection conditions were used without changes for the second group. Partial inversion (i.e., condition $0.7E_b < E_{\rm cal} < E_b$) was used for the third group of selection conditions.

Additional corrections are needed for events in which antineutrons pass through the calorimeter without interaction, and for events with low calorimeter energy $E_{\rm cal} < 0.7E_b$. Due to the large background, these events are ignored in analysis and therefore not available for correction with the procedure described above. Their share in the MC varies from 1.9% at energy $E_b = 945$ MeV to 8.5% at $E_b = 1000$ MeV. It was noted in Section 4 that the contribution from the process of antineutron scattering in the MC must be reduced by a factor of 1.5 in order to describe the shape of the data time spectrum. Upon such a change, the proportion of events with $E_{\rm cal} < 0.7E_b$ in the MC is reduced to 1.4% at $E_b = 945$ to 5.7% at $E_b = 1000$ MeV. The difference between these values is considered additional correction δ_E to the efficiency of detection with an uncertainty of 100%.

Corrections δ_1, δ_2, δ_3, and δ_E, measured according to selection groups, are multiplied by $\delta_t = \delta_1\delta_2\delta_3\delta_E$ and all are given in Table 2. We can see that total correction for efficiency δ_t changes along with energy from 0.8 to 1.25, which is explained by the strong energy dependence of the length ofantineutron absobtion.

The corrected efficiency of detection is obtained from the MC's efficiency by multiplying with total correction δ_t. Values of the corrected efficiency are given along with systemic errors in Table 1. In contrast to our measurements in [1], the corrections at different energy points are not correlated.

7. MEASURED CROSS SECTION $e^+e^- \to n\bar{n}$

Visible cross section $\sigma_{\rm vis}(E) = N_{n\bar{n}}/L\varepsilon$ can be calculated using the number of $n\bar{n}$ events $N_{n\bar{n}}$, luminosity L and efficiency of detection ε (Table 1). Needed Born cross section $\sigma(E)$ is associated with the visible cross in the form

$$\sigma_{\rm vis}(E) = \sigma(E)(1 + \delta(E)) \qquad (6)$$

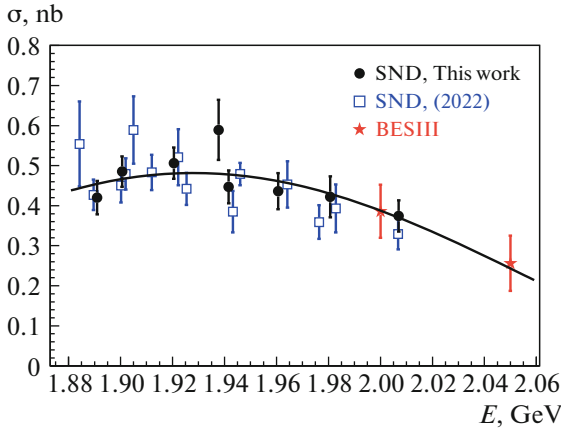

Fig. 7. Cross section $e^+e^- \to n\bar{n}$ measured in this work, compared to SND measurements in [1] and BESIII [2] data. The solid curve is the result from fitting. Only new SND and BESIII data were used in fitting.

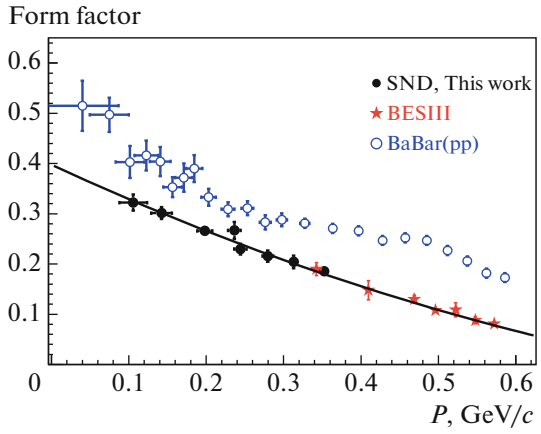

Fig. 8. Measured neutron timelike form factor (black dots) compared to BESIII [2] (red stars) and BABAR [10] proton form factor (blue squares) The solid line is the polynomial fit described in the text.

$$= \int_{-\infty}^{+\infty} G\left(E', E\right) dE'$$

$$\times \int_{0}^{x_{\max}} W\left(s, x\right) \sigma\left(s(1-x)\right) dx,$$

where $W(s,x)$ is the radiator function [9] describing the emission of photons with energy xE_b by initial electrons and positrons, and $G(E',E)$ is a Gaussian function describing the spread of c.m. energy. The contribution from vacuum polarization is ignored in function $W(s,x)$, so our Born cross section is "dressed." Factor $(1+\delta(E))$ considers both radiative corrections and the spread of beam energy. This factor is calculated in each of eight energy points using the Born cross section obtained by fitting the visible cross section using Eq. (6). The energy dependence of the Born cross section is described by Eq. (2), where the neutron effective form factor has the form of a second order polynomial function, as is shown in the next section.

The measured Born cross section is shown in Fig. 7 and listed in Table 1. The dominant contribution to the systemic error is made by the error in correcting the efficiency of detection given in Table 2. Uncertainties in the value of luminosity (1%) and radiative correction (2%) are also considered. The total statistical and systemic error is shown in Fig. 7. Compared to [1], the measured cross section has half the statistical error and a 1.5 times smaller systemic error. At maximum energy $E = 2$ GeV, our cross section is in good agreement with the latest BESIII measurement [2].

8. EFFECTIVE NEUTRON TIMELIKE FORM FACTOR

The effective neutron form factor calculated from the measured cross section using Eq. (2) is listed in Table 1 and shown in Fig. 8 as a function of the antineutron momentum, along with the BESIII data [2] and the proton effective form factor measured in the BABAR experiment [10]. The curve in Fig. 8 approximating the form factor is second order polynomial $|F_n| = a_0 + a_1 p_n + a_2 p_n^2$, in which parameters a_i are obtained by fitting and p_n is the antineutron momentum. The values of parameters are $a_0 = 0.398 \pm 0.022$, $a_1 = -0.713 \pm 0.126$, $a_2 = 0.268 \pm 0.166$. When the fitting curve tends to zero momentum, the expected value of the neutron form factor at the threshold is $a_0 \simeq 0.4$. We can see from Fig. 8 that the form factor for protons is notably larger that the one for neutrons, and their ratio near the threshold is close to 3/2.

9. CONCLUSIONS

We performed an experiment to measure the $e^+e^- \to n\bar{n}$ cross section and the neutron timelike form factor using the SND detector at the VEPP-2000 e^+e^- collider in the 1891 to 2007 MeV region of energies. The measured $e^+e^- \to n\bar{n}$ cross section with energies of 0.4–0.6 nbn agreed with recent SND measurements [1] and had twice the statistical accuracy. At the maximum energy, our cross section agreed with the latest BESIII measurements [2]. The neutron effective timelike form factor was derived from the measured cross section using Eq. (2). Form factor f had energies of 0.3 to 0.2. The value of the form factor for neutrons was notably lower than the one for protons.

FUNDING

This work was supported by the Russian Science Foundation, grant no. 23-22-00011.

CONFLICT OF INTEREST

The authors of this work declare that they have no conflicts of interest.

REFERENCES

1. M. N. Achasov et al. (SND Collab.), Eur. Phys. J. C **82**, 7761 (2022). http://doi.org/10.1140/epjc/s10052-022-10696-0
2. M. Ablikim et al. (BESIII Collab.), Nat. Phys. **17**, 1200 (2021). https://doi.org/10.1038/s41567-021-01345-6

3. P. Yu. Shatunov, D. E. Berkaev, Yu. M. Zharinov, I. M. Zemlyansky, A. S. Kasaev, A. N. Kyrpotin, I. A. Koop, A. P. Lysenko, A. V. Otboev, E. A. Perevedentsev, V. P. Prosvetov, Yu. A. Rogovsky, A. L. Romanov, A. I. Senchenko, A. N. Skrinsky, Yu. M. Shatunov, et al., Part. Nucl. Lett. **13**, 995 (2016).
https://doi.org/10.1134/S154747711607044X
4. M. N. Achasov et al. (SND Collab.), Nucl. Instrum. Methods Phys. Res., Sect. A **449**, 125 (2000).
http://dx.doi.org/10.1016/S0168-9002(99)01302-9
5. M. Astrua, E. Botta, T. Bressani, D. Calvo, C. Casalegno, A. Feliciello, A. Filippi, S. Marcello, M. Agnello, and F. Iazzi, Nucl. Phys. A **697**, 209 (2002).
http://dx.doi.org/10.1016/S0375-9474(01)01252-0
6. M. N. Achasov, V. M. Aulchenko, A. G. Bogdsnchikov, V. P. Druzhinin, V. B. Golubev, A. A. Korol, S. V. Koshuba, D. P. Kovrizhin, S. I. Serednyakov, I. K. Surin, A. I. Tekut'ev, and Yu. V. Usov, J. Instrum. **10**, T06002 (2015).
https://doi.org/10.1088/1748-0221/10/06/T06002
7. A. V. Bozhenok, V. N. Ivanchenko, and Z. K. Silagadze, Nucl. Instrum. Methods Phys. Res., Sect. A **379**, 507 (1996).
8. J. Allison et al. (GEANT Collab), Nucl. Instrum. Methods Phys. Res., Sect. A **835**, 186 (2016).
https://doi.org/10.1016/j.nima.2016.06.125
9. E. A. Kuraev and V. S. Fadin, Sov. J. Nucl. Phys. **41**, 466 (1985).
10. J. P. Lees et al. (BABAR Collab), Phys. Rev. D **87**, 092005 (2013).
http://dx.doi.org/10.1103/PhysRevD.87.092005;
Phys. Rev. D **88**, 072009 (2013).
http://dx.doi.org/10.1103/PhysRevD.88.072009